Title

Structural coupling and magnetic tuning in Mn

2−
x
Co

x
P magnetocalorics for thermomagnetic power generation

Authors

Levin, Emily E
Bocarsly, Joshua D
Grebenkemper, Jason H
et al.

Peer reviewed

Structural coupling and magnetic tuning in Mn$_{2-x}$Co$_x$P magnetocalorics for thermomagnetic power generation

Emily E. Levin,[1, 2] Joshua D. Bocarsly,[1, 2] Jason H. Grebenkemper,[2] Ramsay Issa,[2] Stephen D. Wilson[1, 2] Tresa M. Pollock,[1, 2] and Ram Seshadri[1, 2, 3]

[1)]*Materials Department, University of California, Santa Barbara, CA, 93106, USA*

[2)]*Materials Research Laboratory, University of California, Santa Barbara, CA, 93106, USA*

[3)]*Department of Chemistry and Biochemistry, University of California, Santa Barbara, CA, 93106, USA*[a]

(Dated: 2 March 2020)

Promising materials for magnetic refrigeration and thermomagnetic power generation often display strong coupling between magnetism and structure. It has been previously proposed that MnCoP exhibits this strong coupling, contributing to its substantial magnetocaloric effect near $T_C = 578$ K. Here we show from temperature-dependent synchrotron X-ray diffraction that MnCoP displays a discontinuity in the thermal expansion at T_C, with spontaneous magnetostriction that is positive in the a direction and negative in the b direction, highlighting the anisotropic nature of the magnetostructural coupling. Varying the Mn:Co ratio of Mn$_{2-x}$Co$_x$P within the range $0.6 \leq x \leq 1.4$ allows magnetic properties to be tuned. The T_C decreases as the composition deviates from stoichiometric MnCoP, as does the saturation magnetization. The magnitude of the magnetocaloric effect, $|\Delta S_M|$, decreases as well, due to broadening of the magnetic transition. The large reversible change in magnetization ΔM accessible over a small temperature range under moderate magnetic fields makes these materials promising for thermomagnetic power generation from waste heat.

I. INTRODUCTION

By several estimates, over 60% of all energy produced is rejected as waste heat.[1–4] Low grade waste heat (below 500 K) is usually difficult to recover because other inefficiencies besides the Carnot limit (*eg.* friction) result in heat engines performing very poorly when the temperature difference is small. However, low-grade waste heat constitutes more than 50% of rejected heat; more than 10^4 TWh in the United States alone. If even a small percentage of this energy could be harnessed using economically and environmentally-friendly technologies, this would represent a tremendous new source of green energy. To this end, thermomagnetic power generation has emerged as a promising avenue for the conversion of waste heat into mechanical or electrical power, including for the conversion of very low-grade waste heat, where other technologies such as thermoelectrics are ineffective.[5]

The concept of thermomagnetic generation is closely related to the magnetocaloric effect, which provides a path to energy-efficient and environmentally-friendly refrigeration. In magnetocaloric cooling, a magnetized ferromagnetic material near its Curie temperature is demagnetized adiabatically, leading to an increase in the magnetic entropy (spins are randomized) that is countered by a decrease in the lattice entropy and therefore, the temperature.[6] A thermodynamic cycle for cooling can be implemented by alternating adiabatic and isothermal magnetization and demagnetization, analogous to conventional gas compression cooling.

Conversely, using a temperature difference to traverse the ferromagnetic ordering temperature of a material results in a change in magnetization (ΔM) that can be used to produce useful work.[7] This reverse magnetocaloric effect or thermomagnetic effect is the principle behind thermomagnetic power generators, proposed since the nineteenth century by Tesla[8,9] and Edison.[10,11] Interest in these has recently increased as a variety of promising prototype devices have been built.[12–17] These devices function by cycling the temperature of a magnetic material above and below its transition temperature, leading to changes in magnetization, which are converted into mechanical or electrical energy achieving realistic device efficiencies of around 1% to 3%.[4] Even with these low efficiencies, the ability to recapture abundant and currently unutilized waste heat could result in an enormous new reserve of useful energy. Numerous contributions have described design strategies aimed at higher efficiencies.[3,4,15,16,18–20]

It is advantageous to design materials whose transition temperatures can be controlled around and above room temperature through compositional tuning. While the common figure of merit used for the initial evaluation of a magnetocaloric is $\Delta S_M(T, H)$, the magnetic entropy change experienced by the material upon isothermal magnetization to a certain magnetic field H and at a certain temperature T, for thermomagnetic generators, the reversible change in magnetization $\Delta M(\Delta T, H)$ may be a better metric. As ΔT and H are determined by the specific application (*i.e.* the temperatures of the hot and cold reservoirs available, and the magnetic field achievable), in this contribution we characterize ΔM at a range of temperatures, temperature gradients, and magnetic fields in order to provide a map of the conditions under which the reported materials may be useful. We also note that ΔS_M and ΔM are in fact closely related, as each of these parameters relies on having a sharp magnetic transition.

For magnetocaloric applications, attention has been paid to materials with first-order magnetostructural phase transitions, due to the large (or "giant") magnetocaloric effects possible at these phase transitions, as seen in Gd$_5$(Si,Ge)$_4$,[21]

[a)]Electronic mail: seshadri@mrl.ucsb.edu

(Mn,Fe)$_2$(P,Si,As,Ge),[22–26] La(Fe,Si)$_{13}$,[27,28] and a few other systems. This enhanced magnetocaloric effect arises from magnetostructural coupling, leading to an easily switchable magnetic state and a sharp magnetic transition. However, a first-order transition involves thermal hysteresis and a volume change during the transition, which are especially detrimental to the performance of thermomagnetic generator. Interestingly, magnetostructural coupling can lead to an enhanced magnetocaloric effect even in materials without first-order magnetostructural transitions,[29–31] which is promising for high-performance materials for themomagnetic power generation.

We initially identified MnCoP as a promising material to show strong magnetocaloric effects on the basis of a high-throughput computational search for ferromagnets with strong magnetostructural coupling.[30] This search introduced a simple density functional theory (DFT)-based proxy called the magnetic deformation Σ_M, which is a quantification of the difference of the DFT-optimized unit cells with and without the inclusion of spin polarization in the calculation. This parameter correlates well with experimentally determined values of peak ΔS_M. Σ_M for MnCoP was calculated to be large (3.03%), suggesting the potential for a large magnetocaloric effect near its magnetic Curie temperature of 578 K. Indeed, we measured an experimental peak ΔS_M to be $-6.0 \, \mathrm{J \, kg^{-1} K^{-1}}$ for an applied field of 5 T, which is large for a material without a first-order magnetostructural transition.

Here, we investigate the magnetostructural coupling in stoichiometric MnCoP by monitoring the structure through its magnetic transition temperature using variable-temperature high-resolution synchrotron powder X-ray diffraction. We find pronounced effects on the lattice at the magnetic ordering temperature, helping to explain the notable magnetocaloric effect. In order to establish the application of MnCoP as a material for thermomagnetic power generation, we characterize the solid solution Mn$_{2-x}$Co$_x$P ($0.6 < x < 1.4$) with respect to structural and magnetic properties, finding good agreement with previous observations by Fruchart $et\ al$.[32,33] Mn$_{2-x}$Co$_x$P with $x < 1.6$ forms in the orthorhombic Co$_2$P structure, while $x > 1.6$ forms in the hexagonal Mn$_2$P (Fe$_2$P-type) structure. The maximum saturation magnetization and Curie temperature is found in the stoichiometric MnCoP compound, with both quantities falling off as composition is varied. For $0.68 < x < 0.88$, a metamagnetic transition exists at decreasing temperature for increasing x. The composition Mn$_{1.3}$Co$_{0.7}$P was found to have helical magnetic order at low temperatures.[34] Sun $et\ al$. explored the magnetocaloric response of this composition finding $\Delta S_M = 2.3 \, \mathrm{J \, Kg^{-1} \, K^{-1}}$ for the second-order ferro- to paramagnetic transition near room temperature.[35]

We find that this system allows for the tuning of the Curie temperature between 334 K and 578 K while maintaining substantial ΔS_M and ΔM values, which makes this system a good candidate for these applications. Density functional theory calculations across the solid solution, along with the observed structural and magnetic properties across the series, explain how the magnetic and magnetostructural behavior of the system arises from the behavior of the two transition metal sites in the MnCoP structure.

II. METHODS

Polycrystalline samples of Mn$_{2-x}$Co$_x$P (x = 0.6, 0.7, 0.8, 0.9, 1.0, 1.1, 1.2, 1.4) were prepared from stochiometric mixtures of Mn$_3$P$_2$, Co, and red phosphorus via assisted-microwave preparation,[36] followed by a furnace anneal. The samples were characterized using synchrotron X-ray diffraction (beamline 11-BM, Advanced Photon Source), X-ray fluorescence compositional analysis, and SQUID magnetometry. Details on sample preparation and characterization may be found in the Supplemental Material.

The isothermal magnetic entropy change $\Delta S_M(T,H)$ for each sample was obtained using the `magentro.py` package[29] from magnetization $vs.$ temperature sweeps collected at fixed fields between 0.1 T and 5 T. This method relies on the Maxwell relation $(\partial M/\partial T)_H = (\partial S/\partial H)_T$. The necessary derivatives are calculated using Tikhonov regularization,[37] and then integrated to give $\Delta S_M(T,H)$:

$$\Delta S_M(T,H) = \int_0^H \left(\frac{\partial S}{\partial H} \right)_{H'} \mathrm{d}H' \qquad (1)$$

The same magnetization $vs.$ temperature data was used also used to obtain ΔM, the change in net magnetic moment, as a function of temperature span ΔT, central temperature, and magnetic field.

In addition, the magnetic and magnetostructural coupling behavior of the solid solution Mn$_{2-x}$Co$_x$P was investigated using density functional theory (DFT) as implemented in the Vienna ab-initio Simulation Package (VASP) code[38–40] using a recently described method[41] which involves calculating the magnetic deformation Σ_M on enumerated ordered supercells of the random alloy. Σ_M is a computational proxy that correlates with the strength of magnetostructural coupling, and has been shown to correlate as well with experimental peak ΔS_M.[29] Supercells up to size 24 atoms (two times the primitive TiNiSi-structure cell) were enumerated using the `CASM` code,[42–44] by either substituting Mn atoms onto the Co site in MnCoP ($x < 1$) or by substituting Mn atoms onto the Co site ($x > 1$). More details of the calculations may be found in the Supplemental Material.

III. RESULTS AND DISCUSSION

1. Stoichiometric MnCoP

Rietveld refinement of synchrotron X-ray diffraction data for stoichiometric MnCoP is shown in Figure 1. At room temperature MnCoP adopts the orthorhombic $Pnma$ space group (TiNiSi-type) shown in the inset. This structure is isomorphous with Co$_2$P, while Mn$_2$P forms in the hexagonal Fe$_2$P-type structure.[33] In MnCoP, the cobalt-phosphorous network forms layers of corrugated edge-sharing six-membered rings
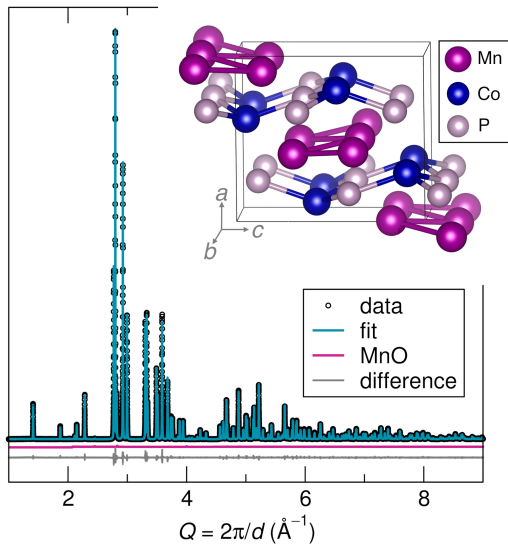
FIG. 1. Synchrotron powder X-ray diffraction of stoichiometric Mn-CoP. The inset shows the MnCoP crystal structure in the *Pnma* space group highlighting the Co-P network in the *bc* plane and the zig-zag manganese chains in the *b* direction.
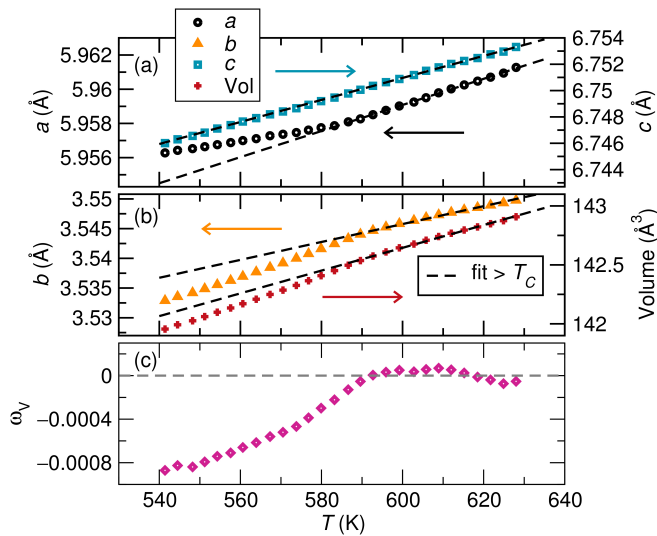

FIG. 2. (a) and (b) show lattice parameters as a function of temperature for MnCoP. Error bars are contained within the points shown. Lattice parameters change linearly with temperature above T_C for the range sampled. There is a kink visible in *a* and *b* near T_C attributed to magnetoelastic coupling. (c) This coupling is quantified by ω_V, the spontaneous volume magnetostriction.

in the *bc* plane with close bond distances (<2.24 Å). These rings are distorted into the half-chair shape described by Landrum, Hoffmann, and co-workers.[45] Each cobalt is tetrahedrally coordinated by phosphorous, while manganese is pyramidally coordinated with bond distances to phosphorous of >2.44 Å. The manganese forms zig-zag chains along the *b* direction with a Mn-Mn nearest neighbor distance of 2.89 Å. Each atom occupies a 4*c* Wyckoff position.

The temperature evolution of the lattice parameters of Mn-

CoP (Figure 2), determined by Rietveld refinement of synchrotron diffraction patterns (Figure S1) at temperatures between 628 K and 538 K reveal highly anisotropic thermal expansion as well as clear anomalies at the magnetic transition ($T_C = 578$ K). Above T_C, the coefficient of thermal expansion in each direction is linear across the data set (r is > 0.995), and is an order of magnitude larger in *b* direction ($\alpha_b = 151$ ppm K^{-1}) than in the *a* or *c* directions ($\alpha_a = 76$ ppm K^{-1}, $\alpha_c = 84$ ppm K^{-1}).

Upon cooling through the magnetic transition, the evolution of the *a* and *b* lattice parameters deviate from this linear trend at T_C, indicating the presence of magnetostructural coupling modifying the nonmagnetic (phonon-driven) thermal expansion of the material, a phenomenon known as spontaneous magnetostriction. Interestingly, the influence of magnetic order is to expand the *a* lattice parameter (positive magnetostriction) while contracting the *b* lattice parameter (negative magnetostriction) and leaving the *c* lattice parameter virtually unchanged. Because the negative effect in the *b* direction is much larger than the positive effect in the *a* direction, the material shows overall a sizable negative spontaneous volume magnetostriction. This is shown in Figure 2(c), quantified as $\omega_V(T) = (V(T) - V_P(T))/V_P(T)$, where $V(T)$ represents the experimentally observed volume and $V_P(T)$ is the volume extrapolated from the paramagnetic regime (*i.e.*, the dotted lines in Figure 2).

Anisotropic coupling between magnetism and structure is also observed in several other promising magnetocalorics, including the Mn,Fe(P,Si) family[46,47] and MnB.[29] In these systems, the anisotropic coupling arises from competition between magnetic and structural degrees of freedom in the structure. After discussing the structural evolution of this system with compositional tuning, we will return to this point in order to provide an explanation for the anisotropic coupling in MnCoP.

2. Compositional tuning

Wavelength dispersive X-ray fluorescence spectroscopy (XRF) confirms that the manganese to cobalt ratio in all samples in the series Mn$_{2-x}$Co$_x$P ($0.6 < x < 1.4$) is the same as the nominal composition, with the exception of $x = 1.4$ which has a composition closer to Mn$_{0.5}$Co$_{1.5}$P. Rietveld refinement of X-ray diffraction determines that all compositions within the sampled range form in the same orthorhombic *Pnma* structure as stoichiometric MnCoP, in agreement with previous studies.[32,33] Some samples have minor amounts of MnO, which is antiferromagnetic below $T_N = 118$ K, as a secondary phase. Properties determined from Rietveld refinement may be found in Table I.

Lattice parameters refined from the diffraction data are shown as a function of composition in Figure 3. The unit cell volume is found to linearly decrease as Co content is increased, as expected by the smaller atomic radius of Co compared to Mn. However, as with the magnetostriction properties, the development of the individual lattice parameters is highly anisotropic. On the Mn-rich side, where Mn atoms
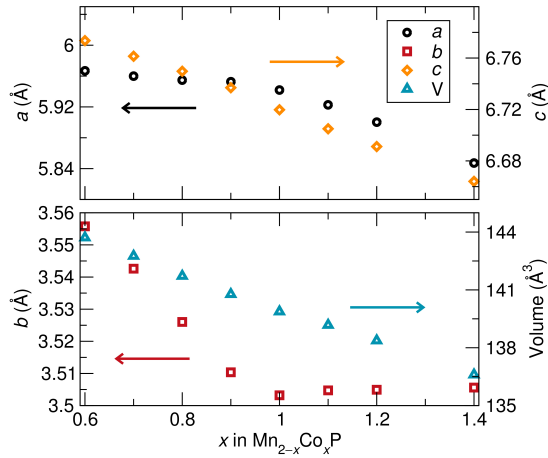
FIG. 3. Lattice parameters of Mn$_{2-x}$Co$_x$P as a function of composition. Error bars are contained within the points. The left side is Mn-rich, and shows a large change in the b lattice parameter with composition, while there is almost no change in a. On the Co-rich side, the a parameter is highly dependent on composition, while b barely changes or even slightly increases despite the addition of a smaller atom. Volume decreases linearly with the addition of cobalt.

TABLE I. Selected crystallographic properties obtained from Rietveld refinement of synchrotron powder XRD of Mn$_{2-x}$Co$_x$P.

x	a (Å)	b (Å)	c (Å)	V (Å^3)	R_{wp} (%)	MnO (wt%)
1.4	5.8473	3.5056	6.6641	136.60	12.10	1.34(6)
1.2	5.9002	3.5049	6.6911	138.37	9.96	3.17(5)
1.1	5.9227	3.5047	6.7050	139.18	8.54	–
1.0	5.9489	3.5032	6.7266	140.18	7.08	0.36(1)
0.9	5.9527	3.5104	6.7370	140.78	12.25	1.24(4)
0.8	5.9547	3.526	6.7497	141.72	9.83	3.75(4)
0.7	5.9599	3.5426	6.7614	142.76	8.34	3.09(3)
0.6	5.9668	3.5558	6.7736	143.71	8.80	2.73(3)

are substituted onto the Co site, a large change in the b lattice parameter with composition is seen, while there is almost no change in a. On the Co-rich side, the a parameter is highly dependent on composition, while b barely changes or even slightly increases despite the addition of a smaller atom. Meanwhile, the c lattice parameter uniformly decreases across the full series.

For $x < 1$, manganese atoms are being introduced into the CoP bonding network of corrugated hexagonal rings in the bc plane. As a result, Mn atoms cause the lattice to expand in the b and c directions (expansions of 3.75% (mol Mn)$^{-1}$ and 1.75% (mol Mn)$^{-1}$, respectively). The a parameter, by comparison, experiences a much smaller expansion of 0.75% (mol Mn)$^{-1}$. In contrast, in the cobalt-rich compounds ($x > 1$) the a parameter decreases much faster than b or c parameters as cobalt is substituted onto the Mn site. Therefore, we can conclude that the intra-layer spacing is controlled primarily by the Mn site, while the in-layer spacing is controlled primarily by the Co site.

This finding allows us to interpret the observed anisotropic magnetostriction in stoichiometric MnCoP. Below T_C we expect the manganese to occupy a larger volume due to the magnetovolume effect, which is based on the theory of itinerant magnetism and therefore occurs in metallic magnets with (at least partly) itinerant character of the magnetism.[48–50] The magnetovolume effect may be thought of as arising from the localization of dispersive electrons into magnetic moments as temperature is cooled. The expanded volume of the Mn site causes the observed positive magnetostriction in the a direction, but has little effect on the in-layer b and c directions. At the same time, there is negative magnetostriction in the b direction, which indicates the presence of an exchange-volume coupling[51] within the Mn-Mn chains that run in the b direction (i.e. the Mn-Mn atoms move towards each other in order to optimize magnetic exchange energy, rather than packing considerations based on ion size).

Magnetization *versus* temperature measurements on this series, shown in Figure 4(a), reveal that all of the samples are ferromagnetic at room temperature except for Mn$_{1.4}$Co$_{0.6}$P, which is antiferromagnetic with Néel temperature of 213 K. The highest T_C is found for MnCoP (578 K), and compositional tuning in either direction allows for the Curie temperature to be brought down to nearly room temperature. In addition, the composition Mn$_{1.3}$Co$_{0.7}$P has a metamagnetic transition at 205 K where it becomes antiferromagnetic below this temperature, as seen by the sudden decrease in magnetization with decreasing temperature. This behavior has been seen previously,[32] and this transition has been investigated for its inverse magnetocaloric effect.[52]

Magnetization *versus* applied field measurements (Figure 4b) reveal that stoichiometric MnCoP possesses the largest total moment at room temperature, and saturation magnetization decreases as composition is changed in either direction. No visible hysteresis is observed for these samples, indicating soft ferromagnetic behavior. Values for T_C and M_{sat} may be found in Table II.

ΔS_M is calculated for the ferro- to paramagnetic transition. ΔS_M for a magnetic field change of 0 T to 5 T is given as a function of temperature for each composition. The ΔS_M peak is narrow for MnCoP, and broadens as composition is varied. Transition temperatures are widely tunable while maintaining significant ΔS_M by varying composition.

ΔM may be considered a more important metric for thermomagnetic generators than ΔS_M. Figure 5(a,c) show the maximum ΔM as a function of the temperature difference at different fixed fields, and (b,d) show maps of ΔM for $\Delta T = 50$ K as a function of temperature and field for two compositions. Data for the other compositions may be found in the Supporting Information Figure S4. MnCoP compares favorably to other non-rare-earth containing second order intermetallics, which range from $\Delta M = 12$ to 40 A m^2 kg^{-1} for $\Delta T = 30$ K.[53]

As discussed in the introduction, the temperature interval over which we calculate ΔM is determined by the application. The operation temperature of a device, as well as the temperature difference between hot and cold reservoirs, must
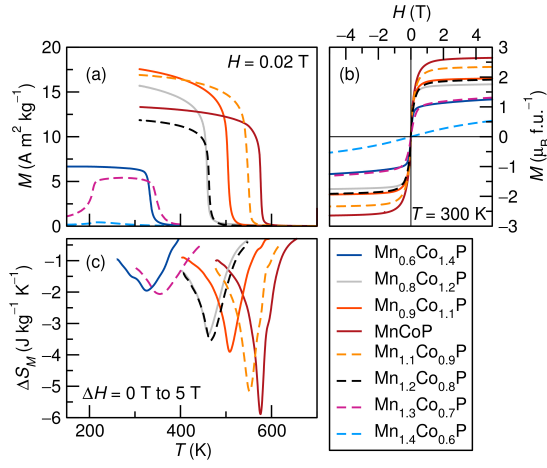
FIG. 4. (a) Field cooled magnetization *versus* temperature and (b) magnetization *versus* applied field show ferromagnetic behavior in all compositions except for Mn$_{1.4}$Co$_{0.6}$P, which is antiferromagnetic. Mn$_{1.3}$Co$_{0.7}$P is metamagnetic, becoming antiferromagnetic at low temperatures. (c) ΔS_M as a function of temperature for all ferromagnetic compositions.

TABLE II. Key magnetic properties of Mn$_{2-x}$Co$_x$P. $-\Delta S_{M,max}$ is the peak value for ΔS_M for a field change $\Delta H = 0\,\mathrm{T}$ to $5\,\mathrm{T}$. Values for ΔM_{max} are given for a 0.5 T field and a temperature interval of $\Delta T = 50\,\mathrm{K}$. T_{center} is the center of the temperature interval for peak ΔM for these same conditions.

x	M_{sat} (μ_B f.u.$^{-1}$)	T_C (K)	$-\Delta S_{M,max}$ (J kg^{-1} K^{-1})	ΔM_{max} (A m^2 kg^{-1})	T_{center} (K)
1.4	1.20	334	1.98	27.98	329
1.2	1.74	460	3.38	36.22	453
1.1	1.94	505	3.92	39.82	499
1.0	2.63	578	5.89	47.87	566
0.9	2.33	550	5.18	49.06	541
0.8	1.90	463	3.57	38.66	458
0.7	1.27	364	2.07	23.35	346

be matched to the material. ΔM increases as the temperature difference is increased, but with diminishing returns for materials with a sharp magnetic transition, such as MnCoP. The transition in Mn$_{0.6}$Co$_{1.4}$P is much broader (as seen in the ΔS_M curve in Figure 4c), and so ΔT must be larger to encompass the minimum and maximum moment states at a given magnetic field.

While ΔS_M increases with increasing field, this is not the case for ΔM in a material with a continuous magnetic transition. When the thermal gradient is low (*i.e.* in applications for thermomagnetic generators), a larger ΔM may be accessed at a smaller fixed field, where the magnetic transition is sharper. In practical applications, it is advantageous for the necessary applied field to be below 1 T because this is readily accessible with permanent magnets.

The magnetic deformation Σ_M was previously calculated for stoichiometric MnCoP,[30] suggesting the presence of strong magnetostructural coupling. Here, we extend these calculations to study the magnetostructural coupling across the solid solution Mn$_{2-x}$Co$_x$P using calculations on enumerated super-
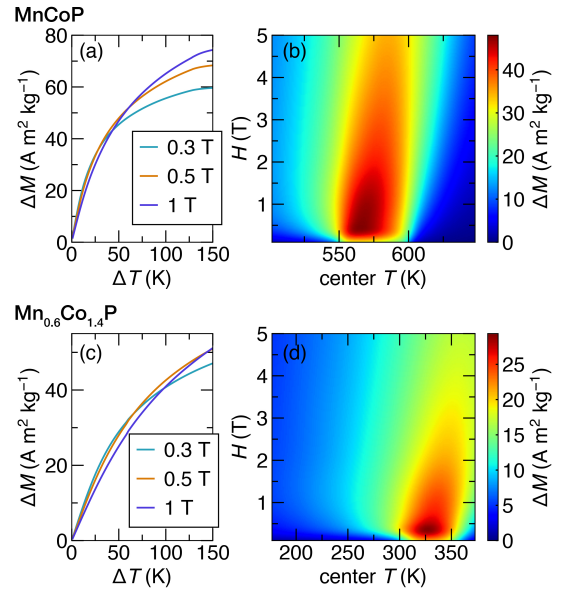

FIG. 5. Maximum ΔM as a function of the temperature difference at several magnetic fields for (a) MnCoP and (c) Mn$_{0.6}$Co$_{1.4}$P. A larger magnetic field will yield a larger ΔM if the temperature difference is large, but for small temperature differences a large field does not give an advantage. (b, d) Color maps of ΔM for $\Delta T = 50\,\mathrm{K}$ as a function of temperature and field for the same compositions. The maximum value of ΔM for $\Delta T = 50\,\mathrm{K}$ is at low field. Center T refers to the center of the temperature interval, or when the hot and cold reservoirs are $\pm 25\,\mathrm{K}$ from center T.
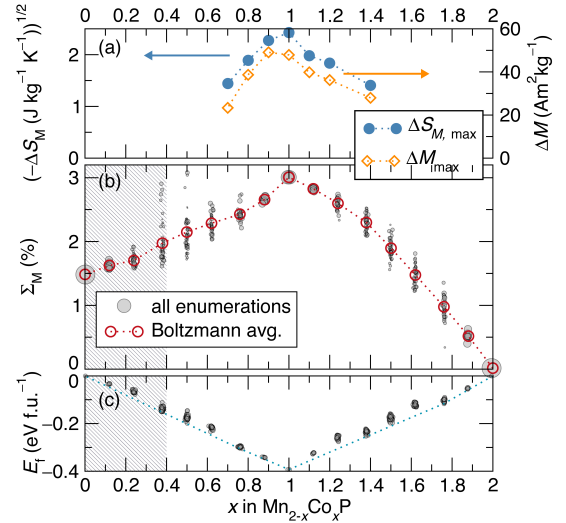

FIG. 6. Comparison between (a) experimental values for maximum $-\Delta S_M$ ($H = 5\,\mathrm{T}$) and peak ΔM ($\Delta T = 50\,\mathrm{K}$) and (b) calculated values of the magnetic deformation Σ_M. In (b), each grey circle represents a single enumerated cell, with the area of each circle proportional to its Boltzmann weight as calculated in equation S3, and the Boltzmann-averaged Σ_M is overlaid. (c) shows the formation energies of the individual ordered unit cells, with the convex hull outlined. In the hatched region, the system is experimentally known to adopt a Fe$_2$P structure type, so these calculations (TiNiSi structure) are not expected to be physical.
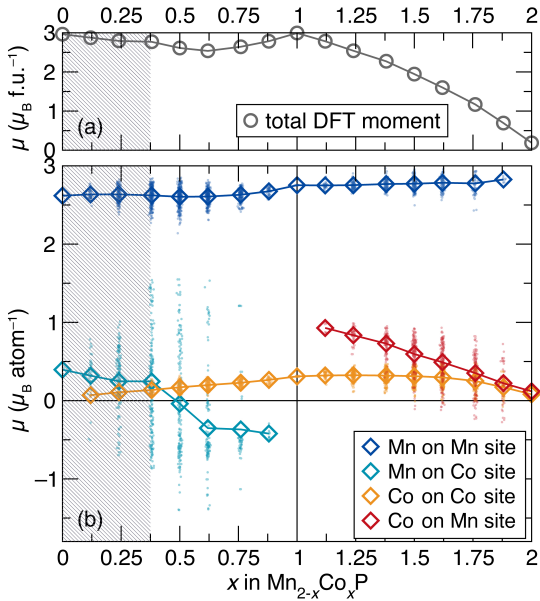
FIG. 7. (a) The Boltzmann-averaged DFT moment as a function of composition. (b) Individual contributions to the moment from each Mn and Co on either atomic site. Each small colored circle represent the moment on each a single atom within one of the enumerated supercells, with the area of the circle proportional to the Boltzmann factor (equation S2) of that supercell. The colored diamonds represent the Boltzmann-averaged moments. In the hatched region, the system is experimentally known to adopt a Fe$_2$P structure type, so these calculations (TiNiSi structure) are not expected to be physical.

cells (Figure 6), as has been recently performed for MnCoGe-based solid solutions.[41] For this study, all enumerated supercells were based on the orthorhombic TiNiSi-type structure of MnCoP. Therefore, the calculations for the very Mn-rich side of the phase diagram, where experimentally a Fe$_2$P-type structure is observed, is not expected to be physical.

Several cells are found to have negative formation energies with respect to Mn$_2$P, MnCoP, and Co$_2$P (Figure 6c), with most other cells within about 20 meV atom^{-1} of the convex hull, supporting the experimentally observed formation of a homogenous solid solution. The maximum Σ_M is found for MnCoP, with the predicted magnetostructural coupling strength smoothly decreasing as the composition is changed in either direction. This calculation corresponds well with the observed peak ΔS_M values (Figure 6a), while the maximum ΔM value for a field of 0.5 T and ΔT of 50 K actually falls slightly on the Mn-rich side of the solid solution, at Mn$_{1.1}$Co$_{0.9}$P. However, the difference in ΔM between the Mn$_{1.1}$Co$_{0.9}$P and MnCoP is very small, and therefore Σ_M performs as a reasonable predictor for ΔM.

At the Co-rich side of the phase diagram, Σ_M falls to 0% for Co$_2$P as the DFT magnetic moment falls to nearly zero, consistent with the experimental observation that Co$_2$P is paramagnetic and does not show ordered ferromagnetism.[54] On the other hand, at $x = 0$, a hypothetical ferromagnetic Mn$_2$P compound with the TiNiSi structure shows stable magnetic moments and a finite Σ_M of 1.5%.

Figure 7 shows the behavior of the local magnetic moments extracted from the enumerated DFT calculations. As expected, the behavior of the local Mn and Co moments depends greatly on the atom identity as well as the site on which it sits. Mn on the Mn site has a nearly constant moment of 2.7 μ_B across the full solid solution, while Co on the Co site shows only a small moment of between 0.1 μ_B and 0.3 μ_B. This large difference in local moment is expected based on the larger size of the Mn site and the presence of strong bonding between the Co-site and P atoms, which competes with the formation of local moments. Indeed, when Co is substituted onto the Mn site it holds an increased moment of up to 1.1 μ_B. However, the local moment of each Co atom on the Mn site decreases as more and more Co is added, eventually yielding the almost nonmagnetic Co$_2$P composition.

On the other side of the series, as Mn is added onto the Co site, it is found to hold a moment of about $-0.4 \mu_B$, with a strong preference for antiparallel orientation to the moments of the Mn site. Analogous behavior has been observed using neutron diffraction in the compound Mn$_{1+x}$Sb, which has the same structure of MnCoP except with vacancies at the Co positions. At finite values of x, Mn interstitials sit on the vacant Co site, and hold moments antiparallel to the larger ferromagnetic Mn atoms on the main site.[55] These calculations explain why the experimentally observed magnetic moment decreases as the composition is varied from MnCoP in either direction. On the Co-rich side, the decrease is caused by replacement of high-moment Mn atoms with lower moment Co-atoms. On the Mn-rich side, conversely, low-moment Co atoms are replaced with higher-moment Mn atoms which orient themselves counter to the ferromagnetic moment and therefore decrease the net moment.

IV. CONCLUSIONS

MnCoP has previously been predicted to have strong magnetostructural coupling (and therefore large $|\Delta S_M|$), and is indeed found to display characteristic discontinuities in the thermal expansion coinciding with the magnetic transition temperature T_C suggestive of such coupling. This is despite the absence of any first-order phase transition. Mn$_{2-x}$Co$_x$P forms a solid solution within the sampled range ($0.6 \leq x \leq 1.4$), allowing magnetic properties to be tuned by varying x. Substitution on the Co site controls the b and c lattice parameters, while substitution on the Mn site controls the a lattice parameter. This is consistent with the positive spontaneous magnetostriction in a observed when MnCoP is cooled through its magnetic transition. T_C, saturation magnetization, and ΔS_M are all largest for stoichiometric MnCoP, but the transition temperature is widely tunable down to nearly room-temperature by varying composition. Changes in $|\Delta S_M|$ trace computed changes of the ensemble-averaged values of Σ_M for the solid solution, underpinning the utility of this proxy. We find ΔM to be large across a range of compositions for $\Delta T = 50$ K, and increasing the temperature differential has a larger effect on the off-stoichiometric materials with broader transitions. The results point to the potential uses of this materials

system for for thermomagnetic power generation.

V. SUPPLEMENTARY MATERIAL

Details of experimental methods and characterization techniques, crystal structure refinement information, x-ray fluorescence analysis of composition, thermal evolution of synchrotron x-ray diffraction, Rietveld fits across compositions, detailed magnetic measurement data, and examples of sample microstructure from scanning electron microscopy.

[1] C. Forman, I. K. Muritala, R. Pardemann, and B. Meyer, "Estimating the global waste heat potential," Renewable Sustainable Energy Rev. **57**, 1568–1579 (2016).

[2] "Estimated U.S. energy consumption in 2018," Lawrence Livermore National Laboratory , LLNL–MI–410527 (2018).

[3] R. A. Kishore and S. Priya, "Low-grade waste heat recovery using the inverse magnetocaloric effect," Sustainable Energy Fuels **1**, 1899–1908 (2017).

[4] R. Kishore and S. Priya, "A Review on Design and Performance of Thermomagnetic Devices," Renew. Sust. Energ. Rev. **81**, 33–44 (2018).

[5] R. Kishore and S. Priya, "A Review on Low-Grade Thermal Energy Harvesting: Materials, Methods and Devices," Materials **11**, 1433 (2018).

[6] V. Franco, J. S. Blazquez, B. Ingale, and A. Conde, "The magnetocaloric effect and magnetic refrigeration near room temperature: Materials and models," Annu. Rev. Mater. Res. **42**, 305–342 (2012).

[7] T. Christiaanse and E. Brück, "Proof-of-concept static thermomagnetic generator experimental device," Metall. Mater. Trans. E **1E**, 36–40 (2014).

[8] N. Tesla, *US Pat.* 396121 (1889).

[9] N. Tesla, *US Pat.* 428057 (1890).

[10] T.A. Edison, *US Pat.* 380100 (1888).

[11] T.A. Edison, *US Pat.* 476983 (1892).

[12] Y. Takahashi, T. Matsuzawa, and M. Nishikawa, "Fundamental performance of the disc-type thermomagnetic engine," Electr. Eng. Jpn. **148**, 26–33 (2004).

[13] Y. Takahashi, K. Yamamoto, and M. Nishikawa, "Fundamental performance of triple magnetic circuit type cylindrical thermomagnetic engine," Electr. Eng. Jpn. **154**, 68–74 (2006).

[14] M. Ujihara, G. Carman, and D. Lee, "Thermal energy harvesting device using ferromagnetic materials," Appl. Phys. Lett. **91**, 093508 (2007).

[15] M. Gueltig, F. Wendler, H. Ossmer, M. Ohtsuka, H. Miki, T. Takagi, and M. Kohl, "High-performance thermomagnetic generators based on Heusler alloy films," Adv. Energy Mater. **7**, 1601879 (2017).

[16] K. Deepak, V. Varma, G. Prasanna, and R. Ramanujan, "Hybrid thermomagnetic oscillator for cooling and direct waste heat conversion to electricity," Appl. Energ. **233-234**, 312–320 (2019).

[17] A. Waske, D. Dzekan, K. Sellschopp, D. Berger, A. Stork, K. Nielsch, and S. Fähler, "Energy harvesting near room temperature using a thermomagnetic generator with a pretzel-like magnetic flux topology," Nat. Energy **4**, 68 (2019).

[18] D. Solomon, "Improving performance of a thermomagnetic generator by cycling magnetic field," J. Appl. Phys. **63**, 915–921 (1988).

[19] V. Srivastava, Y. Song, K. Bhatti, and R. James, "The direct conversion of heat to electricity using multiferroic alloys," Adv. Energy Mater. **1**, 97–104 (2011).

[20] C. Hsu, S. Sandoval, K. Wetzlar, and G. Carman, "Thermomagnetic conversion efficiencies for ferromagnetic materials," J. Appl. Phys. **110**, 123923 (2011).

[21] V. K. Pecharsky and K. A. Gschneidner, Jr., "Giant magnetocaloric effect in Gd$_5$(Si,Ge)$_2$," Phys. Rev. Lett. **78**, 4494–4497 (1997).

[22] O. Tegus, E. Brück, K. Buschow, and F. de Boer, "Transition-metal-based magnetic refrigerants for room-temperature applications," Nature **415**, 150–152 (2002).

[23] E. Brück, O. Tegus, L. Zhang, X. Li, F. de Boer, and K. Buschow, "Magnetic refrigeration near room temperature with Fe$_2$P based compounds," J. Alloy Compd. **383**, 32–36 (2004).

[24] D. Liu, M. Yue, J. Zhang, T. McQueen, J. Lynn, X. Wang, Y. Chen, J. Li, R. Cava, X. Liu, Z. Altounian, and Q. Huang, "Origin and tuning of the magnetocaloric effect in the magnetic refrigerant Mn$_{1.1}$Fe$_{0.9}$(P$_{0.8}$Ge$_{0.2}$)," Phys. Rev. B **79**, 014435 (2009).

[25] N. Trung, Z. Ou, T. Gortenmulder, O. Tegus, K. Buschow, and E. Brück, "Tunable thermal hysteresis in MnFe(P,Ge) compounds," Appl. Phys. Lett. **94**, 102513 (2009).

[26] J. Grebenkemper, J. Bocarsly, E. Levin, G. Seward, C. Heikes, C. Brown, S. Misra, F. Seeler, K. Schierle-Arndt, S.D.Wilson, and R. Seshadri, "Rapid microwave preparation and composition tuning of the high performance magnetocaloric (Mn,Fe)$_2$(P,Si)," Appl. Mater. Interfaces **10**, 7208–7213 (2018).

[27] S. Fujieda, A. Fujita, and K. Fukamichi, "Large magnetocaloric effect in La(Fe$_x$Si$_{1-x}$)$_{13}$ itinerant-electron metamagnetic compounds," Appl. Phys. Lett. **81**, 1276–1278 (2002).

[28] B. G. Shen, J. R. Sun, F. X. Hu, H. W. Zhang, and Z. H. Cheng, "Recent Progress in Exploring Magnetocaloric Materials," Adv. Mater. **21**, 4545–4564 (2009).

[29] J. Bocarsly, E. Levin, S. Humphrey, T. Faske, W. Donner, S. Wilson, and R. Seshadri, "Magnetostructural Coupling Drives Magnetocaloric Behavior: The Case of MnB versus FeB," Chem. Mater. **31**, 4873–4881 (2019).

[30] J. D. Bocarsly, E. E. Levin, C. A. Garcia, K. Schwennicke, S. D. Wilson, and R. Seshadri, "A simple computational proxy for screening magnetocaloric compounds," Chem. Mater. **29**, 1613–1622 (2017).

[31] E. Levin, J. Bocarsly, K. Wyckoff, T. Pollock, and R. Seshadri, "Tuning the magnetocaloric response in half-Heusler/Heusler MnNi$_{1+x}$Sb solid solutions," Phys. Rev. Mater. **1**, 075003 (2017).

[32] R. Fruchart, A. Roger, and J. Senateur, "Crystallographic and Magnetic Properties of Solid Solutions of the Phosphides M_2P, M = Cr, Mn, Fe, Co and Ni," J. Appl. Phys. **40**, 1250–1257 (1969).

[33] R. Fruchart, C. Martin-Farrugia, A. Rouault, and J. Senateur, "Etude structurale et magnétique de CoMnP," Phys. Stat. Sol. **57**, 675–682 (1980).

[34] P. Radhakrishna, H. Fujii, P. Brown, S. Doniach, W. Reichardt, and P. Schweiss, "Magnetic and neutron diffraction studies on (Co$_{1-x}$Mn$_x$)$_2$P," J. Phys.: Condens. Matter **2**, 3359–3368 (1990).

[35] N. Sun, D. Li, S. Xu, Z. Wang, and Z. Zhang, "Room-temperature magnetocaloric effect in (Co$_{0.35}$Mn$_{0.65}$)$_2$P compound," J. Mater. Sci. Technol. **27**, 382–384 (2011).

[36] E. Levin, J. Grebenkemper, T. Pollock, and R. Seshadri, "Protocols for high-temperature assisted-microwave preparation of inorganic compounds," Chem. Mater. **31**, 7151–7159 (2019).

[37] J. J. Stickel, "Data smoothing and numerical differentiation by a regularization method," Comput. Chem. Eng. **34**, 467–475 (2010).

[38] G. Kresse and J. Furthmüller, "Efficient iterative schemes for ab initio total-energy calculations using a plane-wave basis set," Phys. Rev. B **54**, 11169–11186 (1996).

[39] J. P. Perdew, K. Burke, and M. Ernzerhof, "Generalized gradient approximation made simple," Phys. Rev. Lett. **77**, 3865–3868 (1996).

[40] P. E. Blöchl, "Projector augmented-wave method," Phys. Rev. B **50**, 17953–17979 (1994).

[41] C. Garcia, J. Bocarsly, and R. Seshadri, "Computational screening of magnetocaloric alloys," (2019), arXiv:1911.12218 [cond-mat.mtrl-sci].

[42] A. Van der Ven, J. C. Thomas, Q. Xu, and J. Bhattacharya, "Linking the electronic structure of solids to their thermodynamic and kinetic properties," Math. Comput. Simul. **80**, 1393–1410 (2010).

[43] J. C. Thomas and A. Van der Ven, "Finite-temperature properties of strongly anharmonic and mechanically unstable crystal phases from first principles," Phys. Rev. B **88**, 214111 (2013).

[44] B. Puchala and A. Van Der Ven, "Thermodynamics of the Zr-O system from first-principles calculations," Phys. Rev. B **88**, 094108 (2013).

[45] G. Landrum, R. Hoffmann, J. Evers, and H. Boysen, "The TiNiSi family of compounds: Structure and bonding," Inorg. Chem. **37**, 5754–5763 (1998).

[46] N. Dung, Z. Ou, L. Caron, L. Zhang, D. C. Thanh, G. de Wijs, R. de Groot, K. Buschow, and E. Brück, "Mixed magnetism for refrigeration and energy conversion," Adv. Energy Mater. **1**, 1215–1219 (2011).

[47] M. Boeije, P. Roy, F. Guillou, H. Yibole, X. Miao, L. Caron, D. Banerjee, N. van Dijk, R. de Groot, and E. Brück, "Efficient room-temperature cooling with magnets," Chem. Mater. **28**, 4901–4905 (2016).

[48] E. Wohlfarth, "The invar problem," IEEE Trans. Magn. **11**, 1638–1644 (1975).

[49] E. Wohlfarth, "Thermodynamic aspects of itinerant electron magnetism," Phys. B+C **91**, 305–314 (1977).

[50] T. Moriya and K. Usami, "Magneto-volume effect and invar phenomena in ferromagnetic metals," Solid State Commun. **34**, 95–99 (1980).

[51] A. Lindbaum and M. Rotter, "Spontaneous magnetoelastic effects in Gadolinium compounds," in *Handbook of Magnetic Materials*, Vol. 14, edited by K. Buschow (2002) pp. 307–362.

[52] L. Ma, F. Guillou, H. Yibole, X. Miao, A. Lefering, G. Rao, Z. Gu, G. Cheng, and E. Brück, "Structural, magnetic, and magnetocaloric properties of (mn,co)$_2$(si,p) compounds," J. Alloy Compd. **625**, 95–100 (2015).

[53] D. Dzekan, A. Waske, K. Nielsch, and S. Fähler, "Thermomagnetic materials for harvesting low temperature waste heat," arxiv , 1–31 (2020).

[54] S. Fujii, S. Ishida, and S. Asano, "Electronic structures and magnetic properties of fe$_2$p, co$_2$p and comnp," J. Phys. F: Met. Phys. **18**, 971–980 (1988).

[55] A. Taylor, T. Berlijn, S. Hahn, A. May, T. Williams, L. Poudel, S. Calder, R. Fishman, M. Stone, A. Aczel, H. Cao, M. Lumsden, and A. Christianson, "Influence of interstitial mn on magnetism in the room-temperature ferromagnet mn$_{1+\delta}$sb," Phys. Rev. B **91**, 224418 (2015).

Supplementary Information: Structural coupling and magnetic tuning in Mn$_{2-x}$Co$_x$P magnetocalorics for thermomagnetic power generation

Emily E. Levin,[1,2] Joshua D. Bocarsly,[1,2] Jason H. Grebenkemper,[2] Ramsay Issa,[2] Stephen D. Wilson,[1,2] Tresa M. Pollock,[1,2] and Ram Seshadri[1,2,3]

[1] *Materials Department, University of California, Santa Barbara, CA, 93106, USA*

[2] *Materials Research Laboratory, University of California, Santa Barbara, CA, 93106, USA*

[3] *Department of Chemistry and Biochemistry, University of California, Santa Barbara, CA, 93106, USA*[a]

(Dated: 26 February 2020)

[a] Electronic mail: seshadri@mrl.ucsb.edu

SuppInfo: Structural coupling and magnetic tuning in $Mn_{2-x}Co_xP$

I. EXPERIMENTAL METHODS

1. Material preparation

Polycrystalline samples of $Mn_{2-x}Co_xP$ (x = 0.6, 0.7, 0.8, 0.9, 1.0, 1.1, 1.2, 1.4) are prepared *via* assisted-microwave preparation. Stoichiometric amounts of precursor powders Mn_3P_2 (Alfa Aesar, 99%), Co (Sigma-Aldrich, 99.8%), and red phosphorous (Spectrum/Aldrich, 99.99%) are hand ground together in an agate mortar and pestle for 10 min. Well mixed powders are essential due to the short reaction times in the microwave. 300 mg of powder is pressed into a 6 mm pellet using 2 tons of force. Each pellet is sealed in a vitreous silica ampoule under vacuum after flushing 3 times with argon to ensure no oxygen is present. The ampoule is placed in a 20 mL alumina crucible containing 6.5 g activated charcoal (DARCO 12-20 mesh), which is used as a microwave susceptor to initially heat the reactants, such that the sample is buried in the charcoal. The charcoal is first preheated in the microwave for 25 sec. This is to make sure that all reactions start at the same temperature. The crucible is placed in an alumina foam housing off-center on the turntable in the microwave (Panasonic, model NN-SN651B, 1200 W), such that it will rotate through local maxima and minima of electromagnetic radiation within the cavity. Samples are heated at 70% power (840 W) for 2.5 min, and then quenched in air, resulting in a sintered pellet.

The sealed ampoule is annealed in a conventional furnace at 1100°C for 48 h and then air quenched. After the first anneal, the sample is ground again in a mortar and pestle, re-pressed into a 6 mm pellet, and re-sealed in a vitreous silica ampoule before performing this same heat treatment again. This re-grinding and annealing step is found to have a significant influence on magnetic properties, specifically the sharpness of the magnetic transition.

2. Structural characterization

Synchrotron X-ray diffraction data were collected at the 11-BM beamline at the Advanced Photon Source (APS) at Argonne National Laboratory. Room temperature XRD scans using a wavelength of $\lambda = 0.412781$ Å were performed on all samples with a collection time of 1 hour for 2θ 0.5° to 50°. The acquired patterns are analyzed using the

SuppInfo: Structural coupling and magnetic tuning in $Mn_{2-x}Co_xP$

TABLE I. Crystallographic information: Atomic positions of each site in $Mn_{2-x}Co_xP$. The site is referred to by the atom which occupies it in stoichiometric MnCoP. The y coordinate for each site is 0.25. Each atom type occupies a $4c$ Wyckoff position.

x	Mn site			Co site			P site		
	x	z	B_{eq}	x	z	B_{eq}	x	z	B_{eq}
1.4	0.02955(5)	0.83487(5)	0.498(8)	0.14257(5)	0.43554(5)	0.373(8)	0.7640(1)	0.37500(8)	0.48(1)
1.2	0.02908(4)	0.83357(4)	0.427(5)	0.14276(4)	0.43581(4)	0.356(4)	0.76636(8)	0.37450(6)	0.468(7)
1.1	0.02849(4)	0.83298(4)	0.353(5)	0.14255(4)	0.43552(4)	0.234(4)	0.76725(8)	0.37449(6)	0.327(7)
1.0	0.02791(4)	0.83157(4)	0.374(3)	0.14286(3)	0.43549(3)	0.282(3)	0.76782(6)	0.37435(5)	0.288(5)
0.9	0.02777(6)	0.83149(5)	0.401(7)	0.14244(5)	0.43555(5)	0.273(6)	0.76810(9)	0.37471(9)	0.348(9)
0.8	0.02782(4)	0.83128(4)	0.457(5)	0.14372(4)	0.43619(4)	0.335(4)	0.76901(8)	0.37441(6)	0.441(7)
0.7	0.02786(4)	0.83094(3)	0.404(5)	0.14418(3)	0.43642(3)	0.283(5)	0.76936(6)	0.37411(5)	0.390(7)
0.6	0.02762(4)	0.83116(3)	0.367(6)	0.14459(3)	0.43675(3)	0.240(5)	0.77036(7)	0.37374(5)	0.372(8)

Rietveld method in TOPAS Academic to determine crystallographic parameters such as lattice parameters and site occupancy, as well as to identify any secondary phases.[1] Temperature dependent X-ray diffraction data on stoichiometric MnCoP were collected between 2θ of $0.5°$ and $34°$ ($\lambda = 0.414581\,\text{Å}$), leading to a collection time of 10 min per pattern. Temperature was swept at a rate of $0.3°C$/minute such that each pattern is collected over approximately $\Delta T = 3°C$. Temperature was controlled using a calibrated Cyberstar Hot Gas Blower. For data taken while sweeping temperature, patterns were refined sequentially. Crystal structures are visualized using VESTA.[2] Atomic site information for each composition is given in Table I

Microstructure is analyzed using scanning electron microscopy (SEM, Apreo C, FEI, Hillsboro, OR, USA) at 15 keV. Samples are prepared by mounting in epoxy, grinding using SiC paper, and then polishing using diamond suspension down to $1\,\mu$m. Backscattered electron (BSE) imaging is employed to show phase contrast, and energy dispersive X-ray spectroscopy (EDS) to determine local chemical composition. The ratio of Mn to Co is measured using wavelength dispersive X-ray fluorescence spectrometry (XRF, ZSX

TABLE II. Composition of $Mn_{2-x}Co_xP$ measured by XRF.

Nominal x	Measured x
1.4	1.47
1.2	1.20
1.1	1.12
1.0	1.03
0.9	0.92
0.8	0.79
0.7	0.69
0.6	0.62

PrimusIV, Rigaku) in semi-quantitative mode. Values for compositions shown in Table II are calculated assuming that each site is fully occupied.

Some samples are found, by X-ray diffraction and SEM with EDS, to contain trace amounts ($< 1\%$) of quartz SiO_2 or Mn_2SiO_4, which may be the result of reaction with the silica ampules. Pieces of the vitreous silica ampule may have become incorporated when the ampule was broken and the sample was reground before the second heat treatment.

3. *Magnetic property determination*

Magnetic measurements were performed using a magnetic property measurement system (MPMS3, Quantum Design, San Diego, CA, USA) equipped with a vibrating sample magnetometer (VSM/VSM oven). Magnetization (M) *versus* field (H) hysteresis loops were collected at stabilized field set points between $-5\,T$ and $5\,T$. Field cooled magnetization *versus* temperature (T) measurements were performed by collecting continuously while sweeping temperature at a rate of $5\,K/min$ under a magnetic field of $H = 20\,mT$. Measurements above $400\,K$ were performed using an oven attachment. An approximately $3\,mg$ flat piece of sample is attached using alumina cement to a resistively heated sample holder. $\Delta S_M(T, H)$ was determined from series of M vs T measurements through the

SuppInfo: Structural coupling and magnetic tuning in $Mn_{2-x}Co_xP$

ferromagnetic to paramagnetic transitions at fixed magnetic fields between $H = 0.1\,T$ and $5\,T$, with data taken continuously while cooking at a rate of $7\,K\,min^{-1}$. $\Delta S_M(T)$ was then calculated using the following equation,

$$\Delta S_M(T, H) = \int_0^H \left(\frac{\partial M}{\partial T}\right)_{H'} dH' \tag{1}$$

which is derived from the suitable thermodynamic Maxwell relation. The derivatives of magnetization *vs.* temperature curves were calculated using Tikhonov regularization,[3] as previously described in detail by Bocarsly *et al.*[4] These data sets were also used to calculate ΔM as a function of temperature span ΔT, central temperature, and magnetic field.

4. *Density Functional Theory*

The solid solution $Mn_{2-x}Co_xP$ was investigated using density functional theory (DFT) using the method recently described by Garcia *et al.*[5], which involves calculating the magnetic deformation Σ_M[6] on enumerated ordered supercells of the random alloy. The magnetic deformation, which is the degree of lattice deformation between DFT-relaxed unit cells with and without spin-polarization, serves as an indicator of the strength of magnetostructural coupling in a material. Here, 428 individual ordered unit cells with volume up to two times the primitive cell (up to 24 atoms) were generated by substituting Mn atoms onto the Co site in MnCoP ($x < 1$) or by substituting Mn atoms onto the Co site ($x > 1$). This enumeration was performed using the CASM code.[7–9] Structural relaxations with and without spin-polarization were then performed on each structure using the Vienna *ab initio* simulation package (VASP)[10] using the generalized gradient approximation (GGA) exchange-correlation functional as parameterized by Perdew, Burke and Ernzerhof.[11,12] All relaxations were performed starting from the orthorhombic structure of MnCoP, with the magnetic calculations initialized with ferromagnetic moments of $3.0\,\mu_B$ on all the Mn and Co atoms. k-point meshes for the calculations were automatically generated with the number of k-points set to 2500 divided by the number of atoms in the cell. Structural optimizations were performed using the conjugate gradient algorithm with an energy convergence criterion of $10^{-3}\,eV$. The structural relaxations were run iteratively until the volume change between subsequent relaxations was less than 2%. Once this convergence parameter was met, a final electronic optimization was performed for each enumeration while

keeping the structure fixed. The Python packages `pymatgen` and `custodian`[13] were used to automate, monitor, and analyze the VASP calculations.

The magnetic deformation was obtained from the difference in relaxed structures as described in Ref. 14. Then, for each composition x, an ensemble Σ_M value was obtained by a Boltzmann factor-weighted average of the individual cell calculations:

$$w_i = \Omega_i \exp\left(\frac{E_i - E_0}{k_B T}\right) \tag{2}$$

$$\Sigma_{M,\text{Boltzmann}} = \frac{\sum\limits_i w_i \Sigma_{M,i}}{\sum\limits_i w_i} . \tag{3}$$

Here, E_i is the spin-polarized energy of supercell i, expressed *per* 24 atom cell. E_0 is the energy of the lowest-energy enumeration for the composition x, and k_B is the Boltzmann constant. The temperature T was set to $300\,\text{K}$.

In addition, the Boltzmann factor-weighted averages for the values of the local magnetic moments on the Mn and Co atoms on the Mn and Co sites as a function of x were calculated in a similar manner.
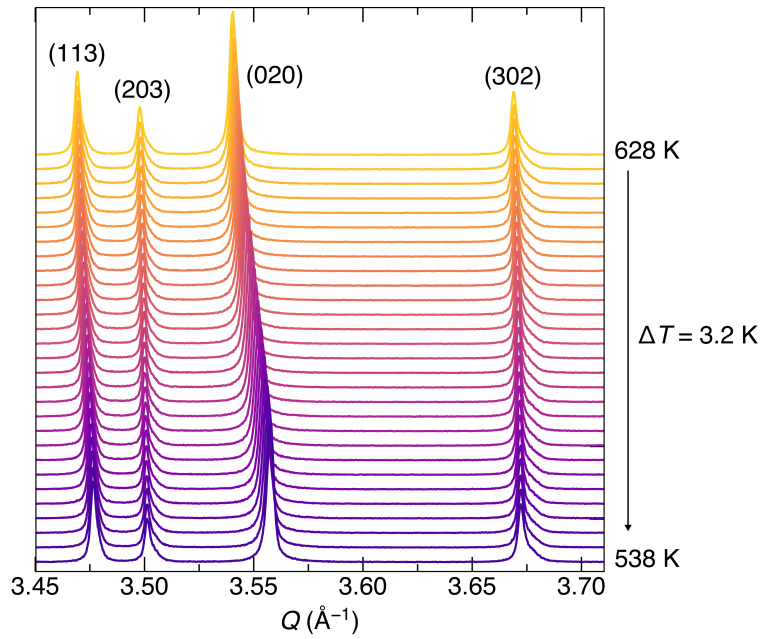
II. SUPPORTING INFORMATION FIGURES

FIG. 1. Portion of synchrotron diffraction patterns of MnCoP as temperature is swept through the magnetic transition from $628\,K$ to $538\,K$. The temperature sweep rate is $0.31\,K\,min^{-1}$ and patterns are collected for $10\,min$ such that each scan is over around $3\,K$. The different thermal evolution of different Bragg peaks highlights the anisotropic thermal expansion and magnetostriction in this material.
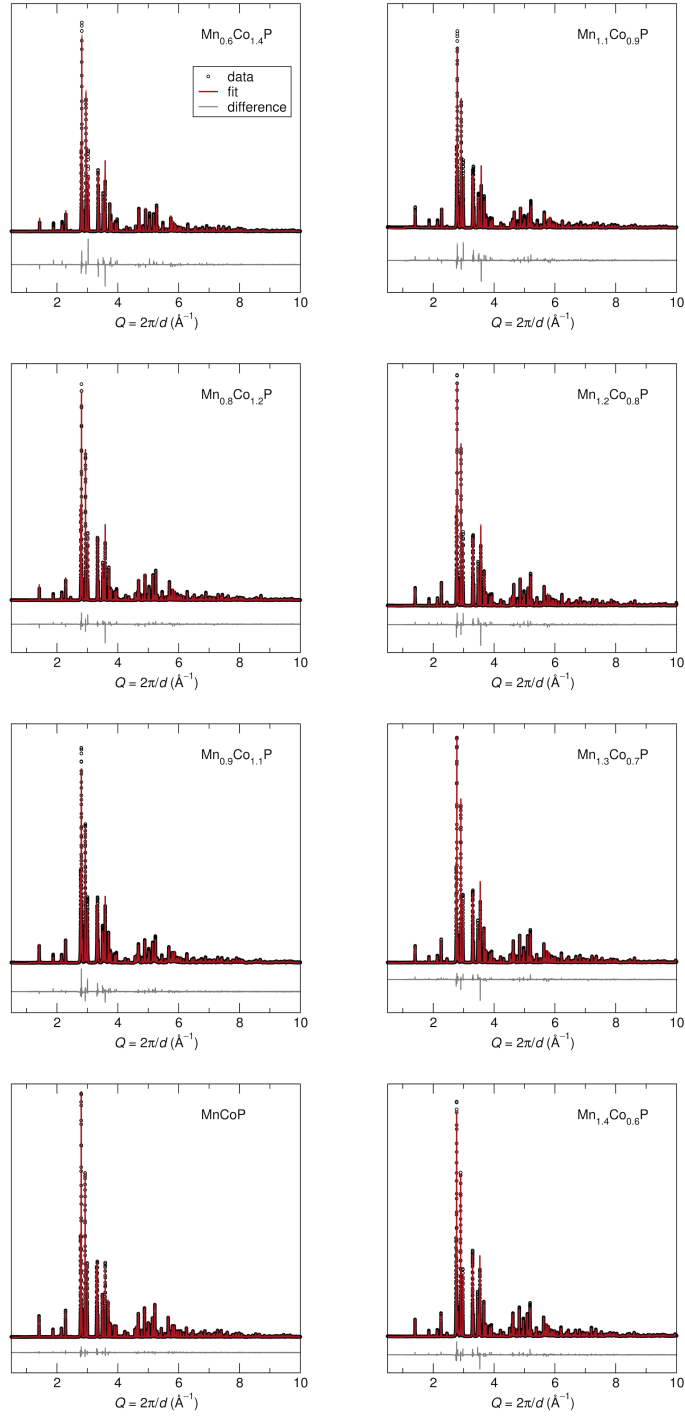
FIG. 2. Rietveld refinements of room temperature synchrotron powder X-ray diffraction data on $Mn_{2-x}Co_xP$ for all explored compositions.
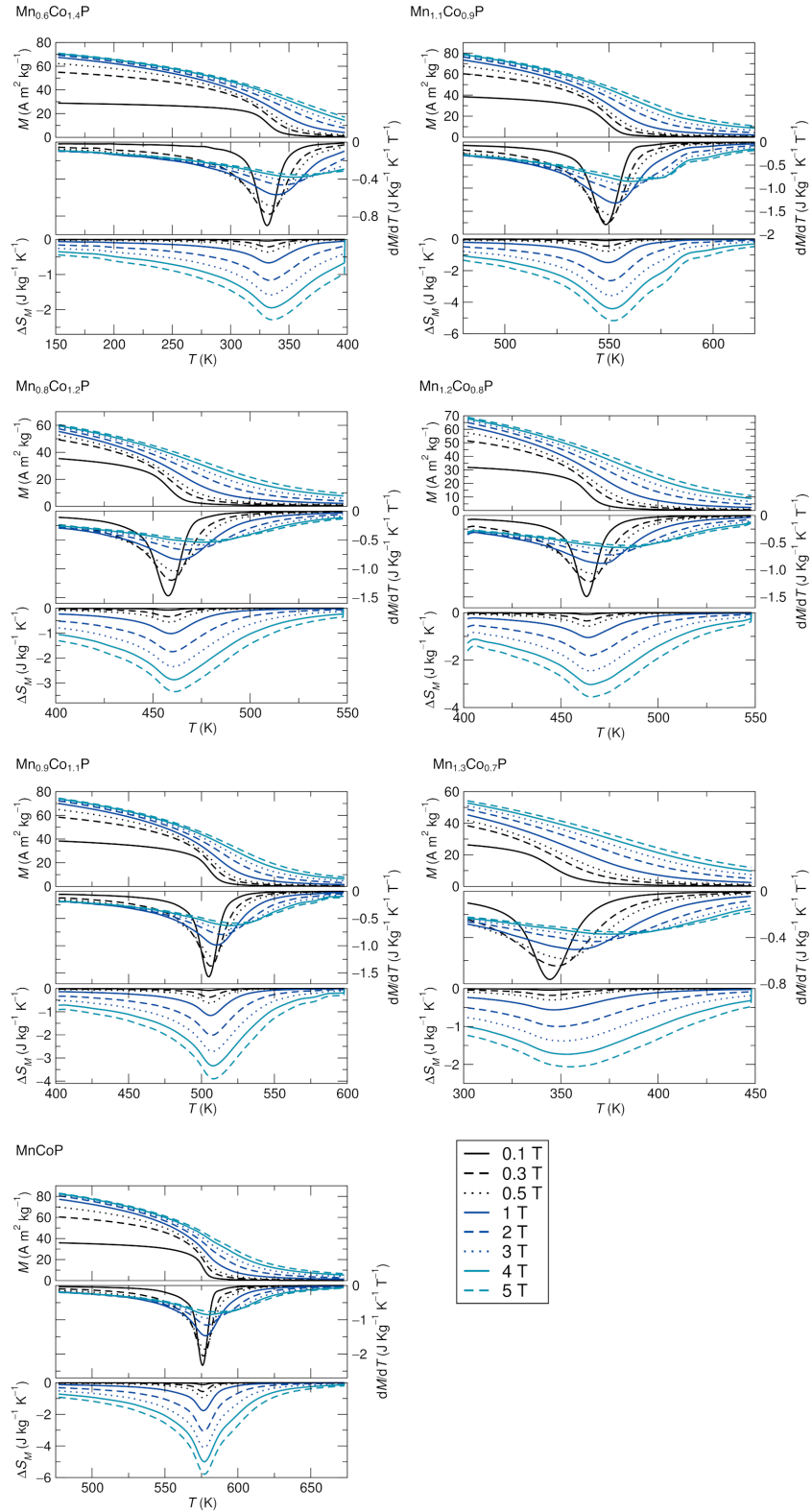
FIG. 3. Magnetization versus temperature measurements encompassing the ferro- to paramagnetic transition were taken at several fields ($H = 0.1\,\mathrm{T}$, $0.3\,\mathrm{T}$, $0.5\,\mathrm{T}$, $1\,\mathrm{T}$, $2\,\mathrm{T}$, $3\,\mathrm{T}$, $4\,\mathrm{T}$, and $5\,\mathrm{T}$) for each composition. In order to calculate ΔS_M these curves are fit, derived to give dM/dT and then integrated with respect to field.
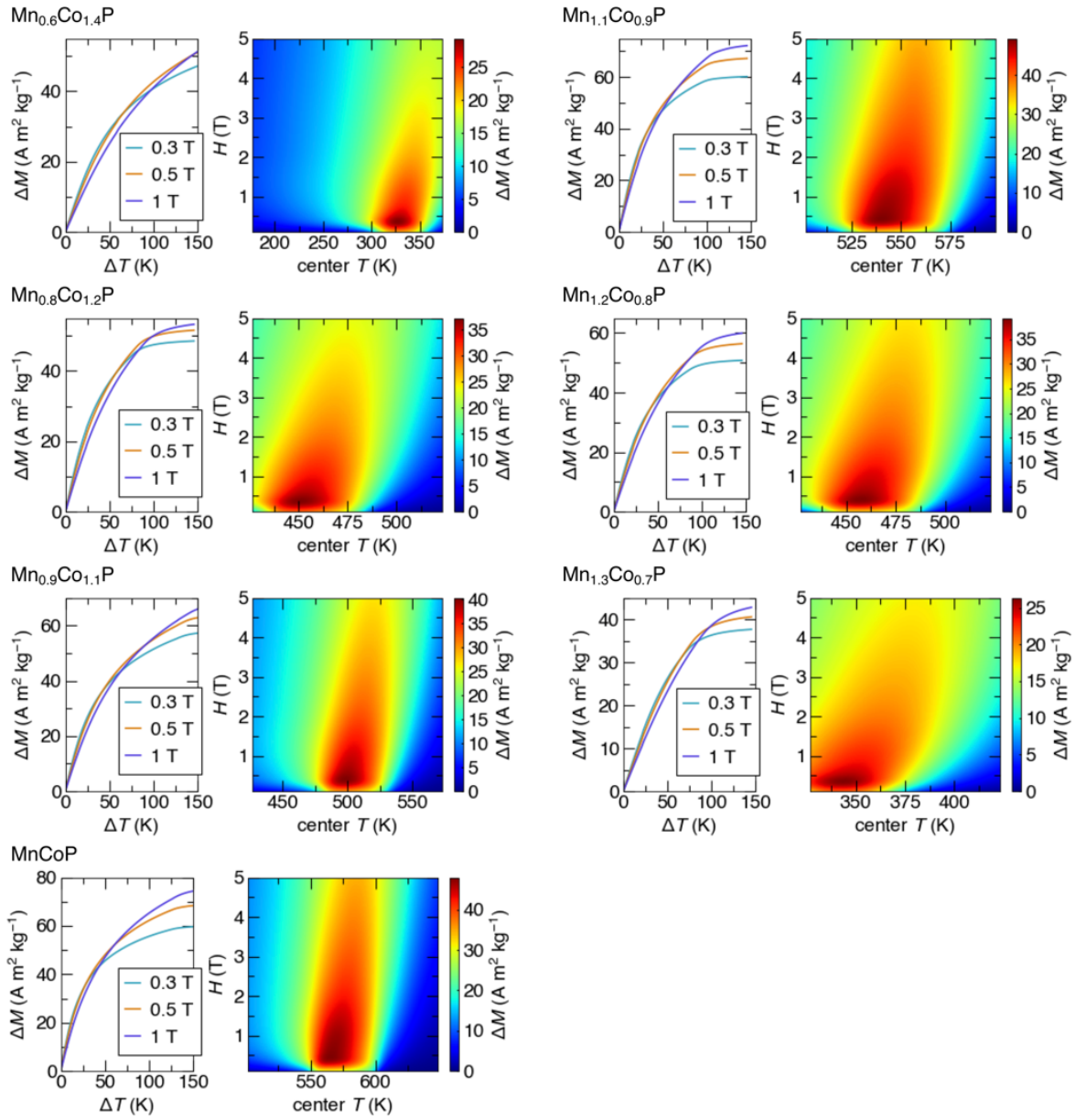
9

FIG. 4. ΔM versus ΔT for each composition, as well as heat maps showing ΔM for each field as a function of temperature for $\Delta T = 50\,K$. For applications with low thermal gradients, or small ΔT, ΔM is maximized for small magnetic fields. This is because the magnetic transition in second order materials broadens as field is increased.
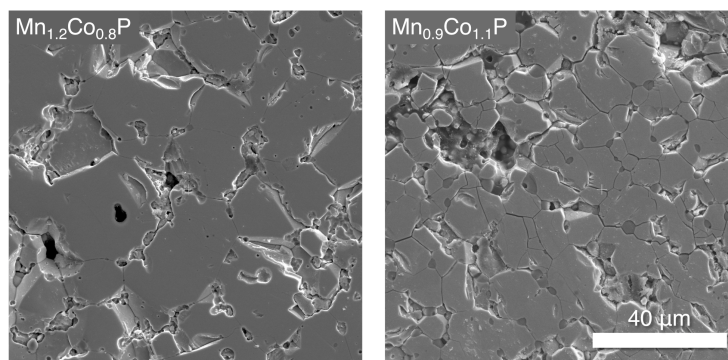
FIG. 5. Scanning electron micrographs comparing representative areas of two samples with compositions (left) $Mn_{1.2}Co_{0.8}P$ and (right) $Mn_{0.9}Co_{1.1}P$. Some particles have pulled out during the grinding and polishing process. These samples are sintered powders. MnO inclusions can be seen at grain boundaries.

REFERENCES

[1]A. Coelho, "Topas Academic V5 Software," `http://www.topas-academic.net/` (2012).

[2]K. Momma and F. Izumi, "VESTA 3 for three-dimensional visualization of crystal, volumetric and morphology data," J. Appl. Crystallogr. **44**, 1272–1276 (2011).

[3]J. J. Stickel, "Data smoothing and numerical differentiation by a regularization method," Comput. Chem. Eng. **34**, 467–475 (2010).

[4]J. Bocarsly, R. Need, S. Wilson, and R. Seshadri, "Magnetoentropic signatures of skyrmionic phase behavior in FeGe," Phys. Rev. B **97**, 100404(R) (2018).

[5]C. Garcia, J. Bocarsly, and R. Seshadri, "Computational screening of magnetocaloric alloys," (2019), arXiv:1911.12218 [cond-mat.mtrl-sci].

[6]J. Bocarsly, E. Levin, S. Humphrey, T. Faske, W. Donner, S. Wilson, and R. Seshadri, "Magnetostructural Coupling Drives Magnetocaloric Behavior: The Case of MnB versus FeB," Chem. Mater. **31**, 4873–4881 (2019).

[7]A. Van der Ven, J. C. Thomas, Q. Xu, and J. Bhattacharya, "Linking the electronic structure of solids to their thermodynamic and kinetic properties," Math. Comput. Simul. **80**, 1393–1410 (2010).

[8]J. C. Thomas and A. Van der Ven, "Finite-temperature properties of strongly anharmonic and mechanically unstable crystal phases from first principles," Phys. Rev. B **88**, 214111 (2013).

[9]B. Puchala and A. Van Der Ven, "Thermodynamics of the Zr-O system from first-principles calculations," Phys. Rev. B **88**, 094108 (2013).

[10]G. Kresse and J. Furthmüller, "Efficient iterative schemes for ab initio total-energy calculations using a plane-wave basis set," Phys. Rev. B **54**, 11169–11186 (1996).

[11]J. P. Perdew, K. Burke, and M. Ernzerhof, "Generalized gradient approximation made simple," Phys. Rev. Lett. **77**, 3865–3868 (1996).

[12]P. E. Blöchl, "Projector augmented-wave method," Phys. Rev. B **50**, 17953–17979 (1994).

[13]S. P. Ong, W. D. Richards, A. Jain, G. Hautier, M. Kocher, S. Cholia, D. Gunter, V. L. Chevrier, K. A. Persson, and G. Ceder, "Python Materials Genomics (pymatgen): A robust, open-source python library for materials analysis," Comput. Mater. Sci. **68**, 314–319 (2013).

[14] J. D. Bocarsly, E. E. Levin, C. A. Garcia, K. Schwennicke, S. D. Wilson, and R. Seshadri, "A simple computational proxy for screening magnetocaloric compounds," Chem. Mater. **29**, 1613–1622 (2017).